Journal of Wind Engineering and Industrial Aerodynamics, 46 & 47 (1993) 21–36
Elsevier

COMPARISON OF VARIOUS TURBULENCE MODELS APPLIED TO A BLUFF BODY

S. MURAKAMI
Professor, Institute of Industrial Science, University of Tokyo,
7-22-1, Roppongi, Minato-ku, Tokyo, 106, Japan

Abstract

Flowfields around bluff bodies are characterized by complex distributions of the strain-rate tensor. Such flowfields can be analyzed with various turbulence models. The shortcoming of the eddy viscosity modelling in the k–ε model is scrutinized in comparison with the results of ASM. The accuracy of the algebraic approximation adopted in ASM is examined using the numerical data given from LES. A new LES model with variable Smagorinsky constant is then presented.

1. INTRODUCTION

Various turbulence models have been proposed as the field of CFD developed, supported by the improvement of CPU hardware. The engineering applications of CFD have also advanced with the development of various turbulence models, e.g. the k–ε two equation model (k–ε), the algebraic second-moment closure model (ASM), the differential second-moment closure model (DSM) and Large Eddy Simulation (LES) etc. The high efficiency and accuracy of these models has been clearly confirmed when applied to such simple flowfields as channel or pipe flows. However their performance is not well established for application to complex turbulent flowfields despite the number of studies made up to the present [1, 2, 3, 4, 5, 6, 7, 10].

Here, three turbulence models, k–ε, ASM and LES, are applied to the flowfield around a bluff body, and thus their relative performances are examined.

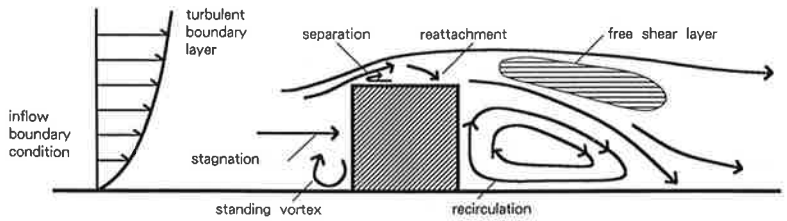

Fig. 1 Flowfield around a cube

2. CHARACTERISTICS OF FLOWFIELD AROUND A BLUFF BODY

The flowfield around a bluff body like a cube placed within the surface boundary is very complicated since it is defined by stagnation, separation, reattachment, circulation and Karman's vortex street etc, as is shown in Fig.1.

Compared to the flowfields traditionally treated in the field of CFD, where rather simple flowfields such as channel or pipe flows were usually dealt with, this is much complicated. The $k-\varepsilon$ turbulence model has attained great success when applied to such simple flowfields, but fails to predict accurately the complex flowfields around bluff bodies such as a cube.

The most distinctive feature of such a complex flowfield is the distribution of the strain-rate tensor $\frac{\partial <u_i>}{\partial x_j}$ which is highly anisotropic and changes significantly depending on the relative position over the bluff body. The distribution of $\frac{\partial <u_i>}{\partial x_j}$ is shown in Fig. 2. There exist various sharp velocity gradients in the streamwise direction as well as in the vertical direction. A simple boundary layer has only one component $\frac{\partial <u_i>}{\partial x_3}$. Since the production of turbulence statistics such as Reynolds stress $<u_i'u_j'>$ is closely related to the strain-rate tensor, the turbulence characteristics around a bluff body become highly complicated because of the complicated distribution of $\frac{\partial <u_i>}{\partial x_j}$, as is explained later in detail.

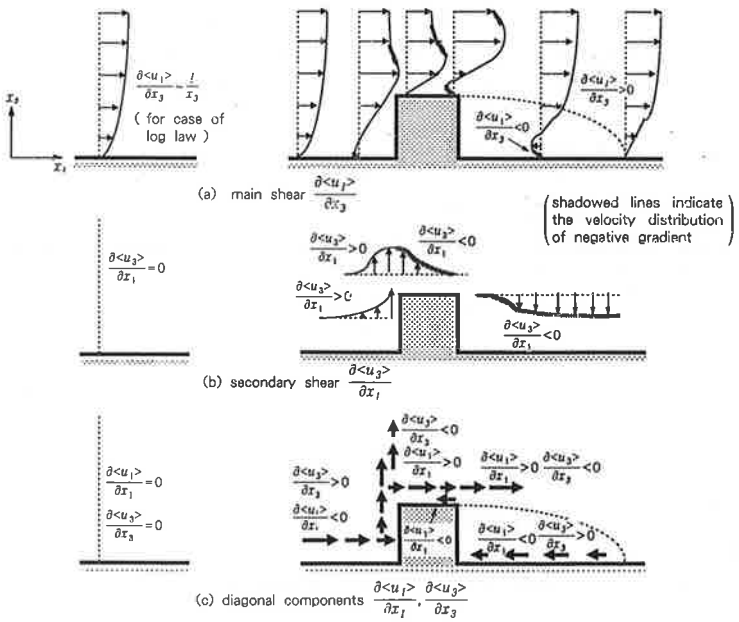

(1) Simple boundary layer (2) Flowfield around a 2D square rib

Fig. 2 Distribution of velocity gradients $\frac{\partial <u_i>}{\partial x_j}$

3. COMPARISON OF MEAN VELOCITY VECTOR FIELD

The mean flowfields around a cube given by wind tunnel testing, $k-\varepsilon$ [11], ASM [15, 16, 18] and LES [13, 14] are compared in terms of mean velocity vectors in Fig. 3. The vertical distributions of velocity behind the model are also shown in Fig. 4. The basic equations for turbulence models are shown in Appendixes 1 ~3. Numerical methods and boundary conditions are described in Notes 1 and 2. Numerical methods and boundary conditions used for the three simulations are made as identical as possible. As shown in Figs. 3 and 4, the correspondences between the experiment and the simulation results given by three turbulence models are fairly good, although small differences are observed in some areas, for example, in the reproduction of separation at the frontal corner. Although each turbulence model seems to give good results for the mean velocity vector field, various discrepancies, including both serious and non-serious ones, are often observed in the results of simulations when we compare the distributions of surface pressure and turbulence statistics in detail, as will be analyzed hereafter.

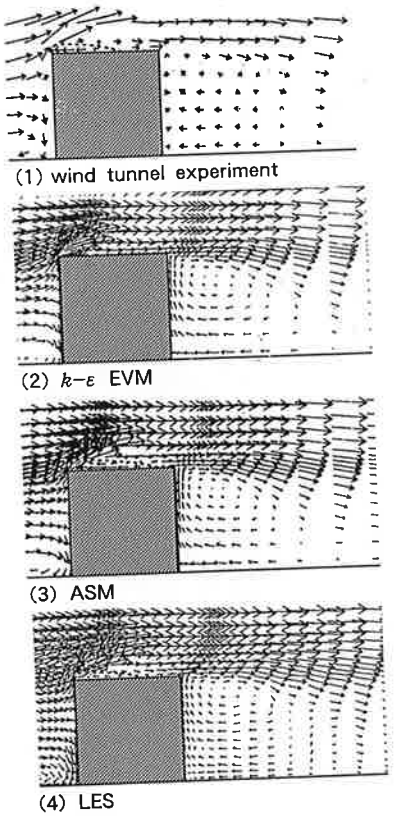

Fig. 3 Distribution of mean velocity vectors (for cube)

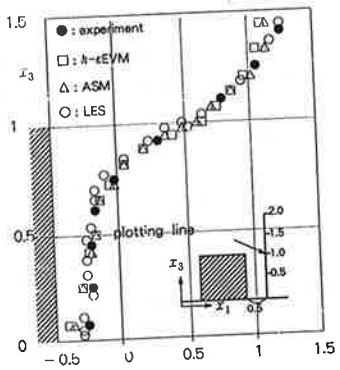

Fig.4 Vertical profiles of $<u_1>$ at center section (for cube)

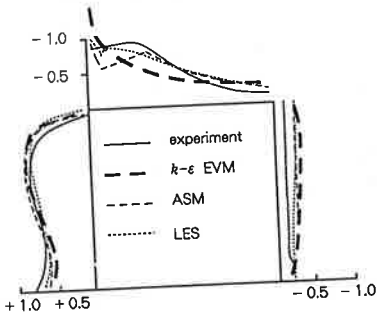

Fig. 5 Distribution of mean pressure coefficient $<C_P>$ (for cube)

4. DISCREPANCY IN SURFACE PRESSURE DISTRIBUTION

The surface pressure distribution for a cube is compared in Fig. 5 [8]. The most important position to be noted is the frontal corner where the largest negative value appears. The result of k–ε deviates greatly at this area. The large negative peak just at the corner decreases rapidly in a distribution peculiar to k–ε. We often get such inaccurate pressure distribution when k–ε is applied to a bluff body. This is caused by the failure to reproduce the small separation here, as is shown in Fig.6, where the area around the frontal corner is magnified. We can observe a small separation in the results of the experiment, ASM and LES, but not in the result of k–ε. It should be noted again that the conditions of the numerics including boundary conditions are made as identical as possible for the simulations of all three turbulence models (cf. Note 2).

The discrepancy of surface pressure peculiar to k–ε is very closely related to the turbulence statistics around the frontal corner. As shown in Fig. 7, turbulence energy k is overestimated in the case of k–ε, which gives rise to a large eddy viscosity ν_t. Hence, the excessive mixing effect produced by this ν_t [6] eliminates the reverse flow on the roof, as is shown in Fig. 6.

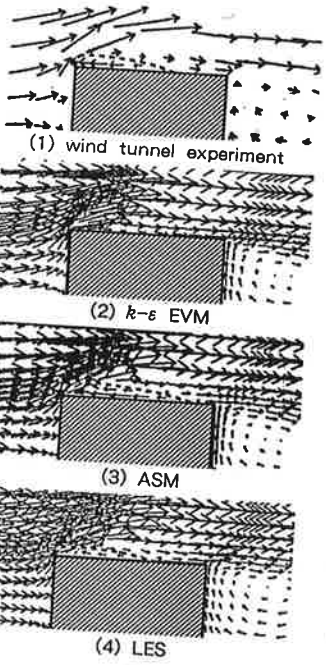

Fig. 6 Same with Fig. 3, but magnified around frontal corner

5. COMPARISON OF k–ε AND ASM ; *modelling of turbulence energy production term* (P_k)

5.1 *Overestimation of turbulence energy k given by k–ε*

One of the most distinct differences between k–ε and ASM (and LES), is the modelling of the production term of turbulence energy P_k ($=-\langle u_i'u_j'\rangle \frac{\partial \langle u_i \rangle}{\partial x_j}$). P_k given by k–ε is based on eddy viscosity modelling (EVM) (cf. eqs.(1.5) and (1.6) in Appendix 1) and that given by ASM is calculated according to the exact expression

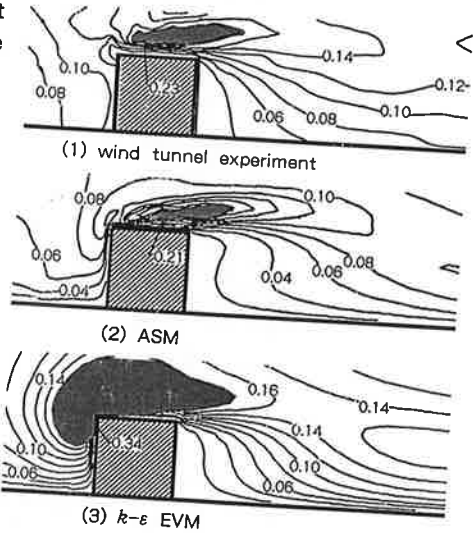

Fig.7 Distribution of k (for 2D square rib)

of P_k (cf. eq.(2.9) in Appendix 2).

The distributions of k given by $k-\varepsilon$ and ASM are illustrated for the flowfield around a 2D square rib in Fig. 7. The $k-\varepsilon$ model greatly overestimates the value of k around the frontal corner. The result of ASM agrees very well with that of the wind tunnel test.

The mechanism of overestimation of k by $k-\varepsilon$ is scrutinized here. P_k is composed of $P_{k\cdot n}$ and $P_{k\cdot s}$ as is shown in Fig. 8, where $P_{k\cdot n}$ means the turbulence production by diagonal components of the strain-rate tensor and $P_{k\cdot s}$ is that given by off-diagonal elements.

In general, the magnitude of $P_{k\cdot n}$ does not become so large in the cases of ASM or LES, since $P_{k\cdot n}$ is calculated using the exact form of eq.(1) in Fig. 8, which is expressed as the subtraction of $<u_1'^2>$ and $<u_3'^2>$. On the other hand, the turbulence production due to $<u_1'^2>$ and $<u_3'^2>$ is simply added in the case of $k-\varepsilon$ EVM as expressed by eq.(2) in Fig. 8 and thereby the value of $P_{k\cdot n}$ becomes very large . This erroneous expression is the fallacy given by eddy viscosity modelling [9, 20].

This overestimation of k caused by the diagonal elements of the strain-rate tensor is the fundamental shortcoming of EVM when it is applied to a flowfield involving impinging where usually large values of $\frac{\partial <u_i>}{\partial x_i}$ exist, as is shown in Fig. 2. The analysis of the distribution of $\frac{\partial <u_i>}{\partial x_j}$ is thus very important since it controls the values of production of Reynolds stresses. The overestimation of $P_{k\cdot s}$ also occurs in the case of $k-\varepsilon$ EVM. The mechanism of overestimation can be shown easily by the same manner as $P_{k\cdot n}$ as is shown in Fig. 8.

The distributions of P_k, $P_{k\cdot n}$ and $P_{k\cdot s}$ are shown in

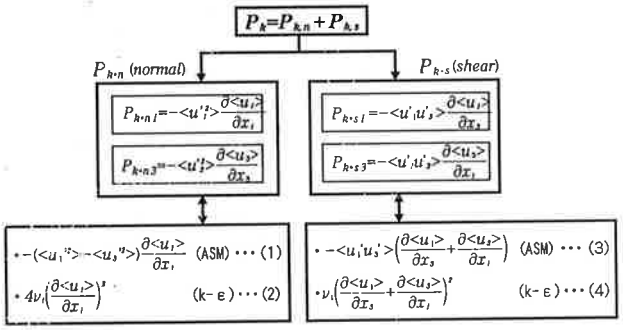

Fig. 8 Calculation of P_k by $k-\varepsilon$ and ASM (for 2D)

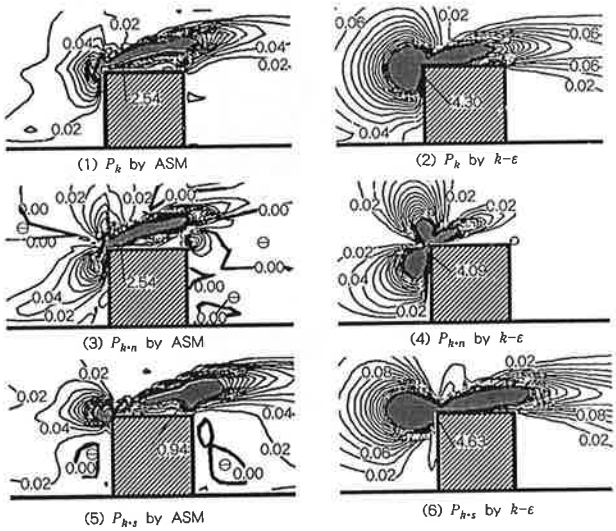

Fig. 9 Comparison of P_k , $P_{k\cdot n}$ and $P_{k\cdot s}$ for $k-\varepsilon$ and ASM (for 2D square rib, ⊖ indicates area with negative value)

Fig. 9. These distributions are closely correlated with the distribution of $\frac{\partial<u_i>}{\partial x_j}$ illustrated in Fig. 2. In the case of ASM, the values of $P_{k\cdot n}$ and $P_{k\cdot s}$ show negative values in some areas, and they are subtracted from each other in those areas, e.g. in the area around the frontal corner. Thus the value of P_k given by ASM does not become so large as that given by k-ε. However the fallacy given by EVM always gives a positive value for $P_{k\cdot n}$ and $P_{k\cdot s}$ in the case of k-ε, as is shown in Fig. 8, and thereby the value of k is overestimated.

5.2 Interaction between each component of P_{ij} and $<u_i'u_j'>$

A comparison between $<u_1'u_3'>$ and P_{13} is shown in Fig. 10. The distributions of the two values correspond very well with each other, for example, the correspondence of positive zone and negative zone etc. This is a natural result when the physical relation between the two is considered. Such a close relation is also given for the cases of other components. i.e. $<u_1'^2>$ and P_{11} , $<u_3'^2>$ and P_{33}.

Thus, the distributions of Reynolds stresses $<u_i'u_j'>$ are well controlled by the distributions of P_{ij}. Thus it is very important to know the distribution of P_{ij} in order to analyze the turbulent properties around a bluff body. Here we propose a new zoning of the flowfield around a bluff body based on the property of P_{ij}, as is shown in Fig.11. This zoning is greatly different from the traditional zoning of the flowfield around a cube, as is shown in Fig. 1. The sign of each term of P_{ij} changes according to the signs of $<u_i'u_j'>$ and $\frac{\partial<u_i>}{\partial x_j}$. The distributions of Reynolds stress $<u_i'u_j'>$ can be well comprehended with the aid of this zoning.

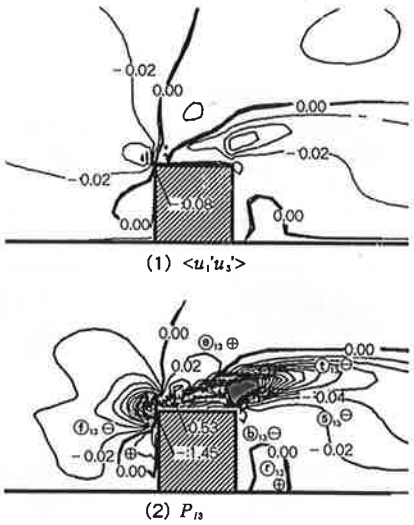

Fig. 10 Correspondence between distributions of $<u_1'u_3'>$ and P_{13} (by ASM, for 2D)

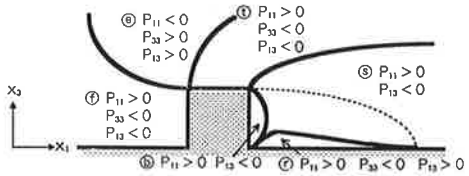

Fig. 11 New zoning of flowfield based on the property of P_{ij} (for 2D)

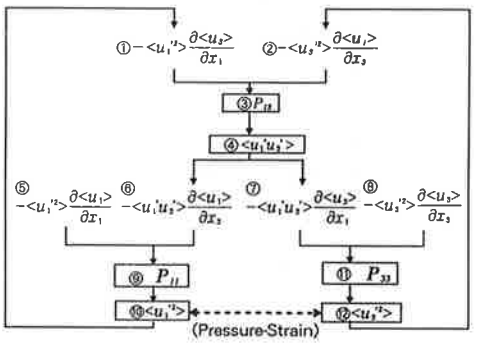

Fig. 12 Interaction diagram of each component of $<u_i'u_j'>$ and P_{ij} (for 2D

Furthermore, components of $\langle u_i'u_j'\rangle$ interact with each other through P_{ij}. An interaction diagram is shown in Fig. 12. For example, $\langle u_1'^2\rangle$ and $\langle u_3'^2\rangle$ contribute to the production of $\langle u_1'u_3'\rangle$ through $P_{13}=-\langle u_1'^2\rangle\frac{\partial\langle u_3\rangle}{\partial x_1}-\langle u_3'^2\rangle\frac{\partial\langle u_1\rangle}{\partial x_3}$. The production of $\langle u_1'^2\rangle$ (*i.e.* $P_{11}=-2\langle u_1'^2\rangle\frac{\partial\langle u_1\rangle}{\partial x_1}-2\langle u_1'u_3'\rangle\frac{\partial\langle u_1\rangle}{\partial x_3}$) is contributed from $\langle u_1'^2\rangle$ itself and $\langle u_1'u_3'\rangle$. The k–ε model is very poor at reproducing the anisotropic property of each component of $\langle u_i'u_j'\rangle$ since it is based on isotropic eddy viscosity modelling.

6. COMPARISON OF ASM AND LES ; *modelling of convection and diffusion terms*

6.1 *Discrepancies observed in the distributions of* $\langle u_i'^2\rangle/2k$ *given by ASM*

The reproduction of the anisotropic property of each component of normal stress $\langle u_i'^2\rangle$ is examined in Figs. 13～15, where distributions of $\langle u_i'^2\rangle/2k$ are presented as a measure by which to judge the anisotropy of turbulence.

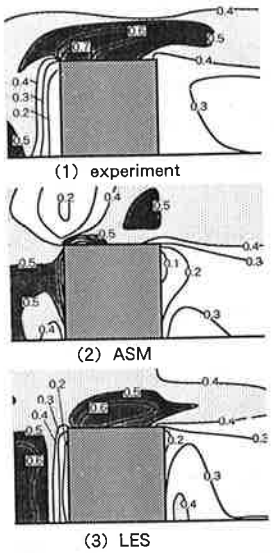

Fig.13 Distributions of $\langle u_i'^2\rangle/2k$

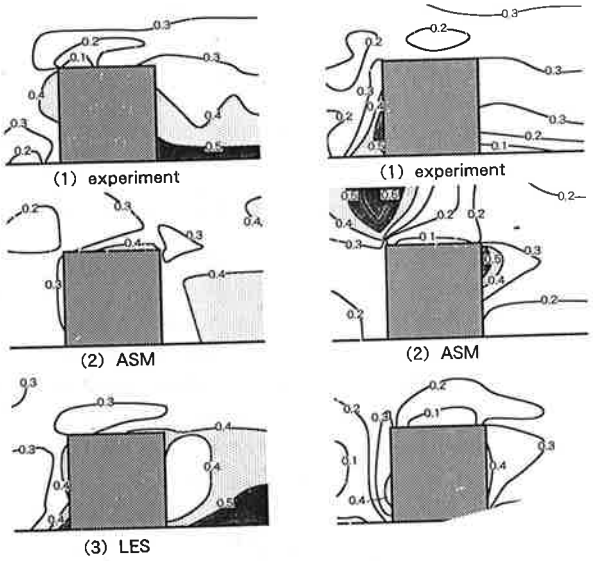

Fig.14 Distributions of $\langle u_i'^2\rangle/2k$

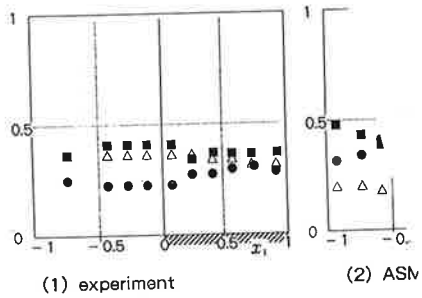

Fig. 16 Longitudinal profiles o

ndary

The orizontal
Here experiments,

This is the C_{s0},tress turbulence
Eq.(4.13) is tran here
$\overline{C_s}=1-C_{s0}$ gy, Report No.TFD/

by means of LES and
near Flows (1991).

The results of the wind tunnel experiment illustrate that the value of $\langle u_1'^2 \rangle$ dominates in the area on the roof and in the downstream free shear layer (Fig. 13). In the recirculation region behind the cube, $\langle u_2'^2 \rangle/2k$ has a large value where Karman's vortex shedding appears (Fig. 14). The value of $\langle u_3'^2 \rangle/2k$ is the smallest in general, except for the region in the vicinity of the windward face where $\langle u_3'^2 \rangle$ is the largest component (Fig.15).

The anisotropic features given by each component of $\langle u_i'^2 \rangle/2k$ in LES correspond very well with those of the experiment (Figs.13 ~15).

The results of ASM show serious discrepancies in the area above the frontal corner in comparison with both the experiment and LES. In this area, the results of ASM show abnormal maximum and minimum peaks in the distributions of $\langle u_3'^2 \rangle/2k$ and $\langle u_1'^2 \rangle/2k$ respectively (cf. Figs. 13, 15, 16), as is identically observed in the results of k–ε EVM. These peaks do not appear in the results of the experiment and LES. The cause of these discrepancies is examined below.

6.2 *Inaccuracy in the algebraic approximation used in ASM*

In the formulation of ASM, the convection term C_{ij} and diffusion term D_{ij} of the transport equation of $\langle u_i'u_j' \rangle$ is approximated by algebraic expression, e.g. $-(C_{ij}-D_{ij})$ is substituted by $-\langle u_i'u_j' \rangle \frac{(P_k-\varepsilon)}{k}$, as is shown in eq.(2.6) in Appendix 2.

It is well known that this algebraic expression is most effective when the values of $\frac{\langle u_i'u_j' \rangle}{k}$ are almost constant across the flowfield. However, Figs.13 ~16 indicate that the values of $\frac{\langle u_i'u_j' \rangle}{k}$ are not constant. $\langle u_i'u_j' \rangle$ and k vary in very different manners in the flowfield around the cube, particularly in the area around the frontal corner. Thus, the results from ASM are unavoidably inaccurate because of the algebraic approximation used for $-(C_{ij}-D_{ij})$ in this area. The inaccuracy in ASM is clearly observed near the frontal corner in the horizontal distributions of $\langle u_3'^2 \rangle/2k$ (Fig.16).

Lastly, the balance of production term P_{33} and convection and diffusion terms $-(C_{33}-D_{33})$ in the transport equation for $\langle u_3'^2 \rangle$ is discussed in order to examine the large difference observed in the distributions of $\langle u_3'^2 \rangle/2k$ in the results of ASM and LES. In this area the velocity gradient $\frac{\partial \langle u_3 \rangle}{\partial x_3}$ has a large negative value, since a large positive value of $\langle u_3 \rangle$ is produced related to the impinging at windward wall and decreases in the vertical direction as is illustrated in Figs. 2 and 3. This large negative value of $\frac{\partial \langle u_3 \rangle}{\partial x_3}$ makes the value of P_{33} very

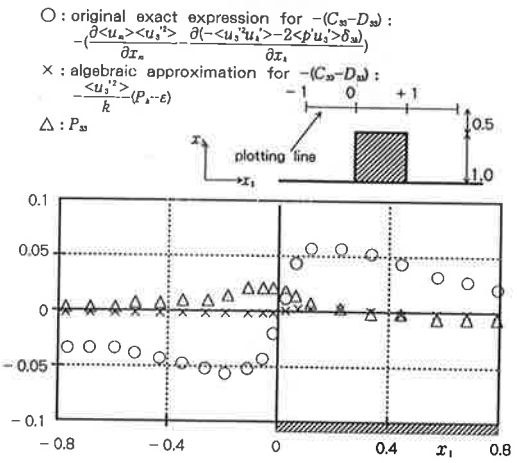

Fig.17 Distributions of $-(C_{33}-D_{33})$ and P_{33} above the roof estimated using numerical data given from LES

large in comparison with those of P_{11} and P_{22} which do not include the term containing $\frac{\partial \langle u_3 \rangle}{\partial x_3}$. Consequently the anisotropic property of turbulence is strongly influenced by the value of P_{33} in this area. Fig. 17 shows a comparison between the value of P_{33} and two types of $-(C_{33}-D_{33})$. One $-(C_{33}-D_{33})$ is estimated from the original exact expression and the other is given by the algebraic expression introduced in ASM, both using numerical data from LES. It is found that $-(C_{33}-D_{33})$ estimated from the original exact expression has a large negative value in the area where the distribution of P_{33} indicates a maximum peak, so the increase of $\langle u_3'^2 \rangle$ caused by the positive value of P_{33} is restrained by the effect of $-(C_{33}-D_{33})$. This means that $\langle u_3'^2 \rangle$ increased by P_{33} is efficiently convected and diffused to the downstream and upper sides of the flowfield, so that the distribution of $\langle u_3'^2 \rangle / 2k$ does not have a sharp peak in the area in front of the windward corner in the experiment and LES (Figs. 15, 16, 17). As is clearly shown in Fig. 17, the approximation adopted in ASM cannot reproduce this strong effect of convection and diffusion, which should decrease $\langle u_3'^2 \rangle$ in this area. This inaccurate estimation of $-(C_{33}-D_{33})$ causes an overly large value of $\langle u_3'^2 \rangle$ in the case of ASM. This error is a fundamental shortcoming of ASM, and is likely to become clear in areas where the distribution of $\frac{\partial \langle u_i \rangle}{\partial x_j}$ is very complicated and significantly large values of C_{ij} and D_{ij} exist non-uniformly.

7. IMPROVEMENT OF LES ; new SGS model with variable Smagorinsky constant

In the formulation of LES, the Smagorinsky subgrid-scale (SGS) model is adopted here, as is shown in Appendix 3. The Smagorinsky SGS model is a kind of eddy viscosity model with Smagorinsky constant C_S. Here we would like to explore an improvement of that model. In the usual LES simulation, the Smagorinsky constant C_S is set to be constant with time and space. Here, C_S is set to be 0.12. However, the value of C_S should be changed according to the property of the flowfield. An optimized value of C_S is proposed for various flowfields, e.g. C_S=0.1 for channel flow and C_S=0.23 for isotropic decay flow.

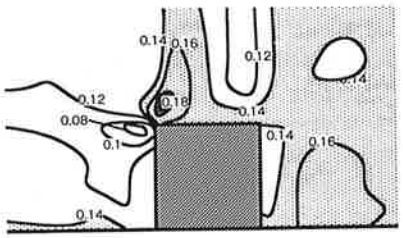

Fig. 18 Distribution of Smagorinsky constant $\langle C_S \rangle$ (by LES with new model)

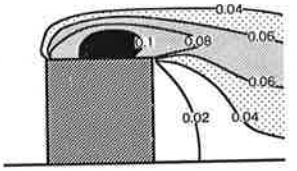

(1) wind turnnel test

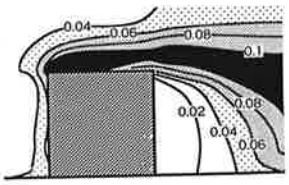

(2) $C_S = 0.12$

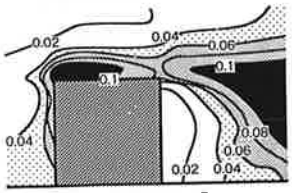

(3) with variable C_S

Fig. 19 Distributions of k (by LES)

Since the flow property around a bluff body changes greatly as was describe in detail above, the value of C_s should be changed according to the flow propert peculiar to the relative position over the bluff body. The optimum value of C_s ma be as follows ; $C_s \fallingdotseq 0.1$ in the upwind area apart from the model (optimized valu for channel flow), $C_s \fallingdotseq 0.16$ in the recirculating region behind the model (optimize value for room airflow) and C_s=0.12~0.15 in the downstream free shear layer cf. Fig. 1).

In the new model for Smagorinsky constant, C_s [22, 23] is given for each position and for each time step, according to the flow property following eq.(3 8) in Appendix 3.

In the original Smagorinsky model, C_s is derived basing on the assumption of local equilibrium for k_{sgs} (SGS value of turbulence energy k, cf. Appendix 4). This assumption does not apply well to the flowfield around a bluff body, where the flow property changes so greatly.

Thus in the new model presented here, the assumption of local equilibrium is not adopted and C_s is derived based on the transport equation of k_{sgs}, as is shown in Appendix 4, where the effects of advection and diffusion are incorporated.

The optimized value of C_s around a cubic model is illustrated in Fig. 18, based on the new model. Estimated value of C_s in each area corresponds well to the various values of C_s previously optimized (i.e. 0.1 for channel flow, 0.16 for room airflow etc), reflecting the characteristics of the flowfield through the value of $S(=\left[\frac{1}{2}\left(\frac{\partial u_i}{\partial x_j}+\frac{\partial u_j}{\partial x_i}\right)^2\right]^{1/2})$.

A comparison of turbulence energy k is shown in Fig. 19. In the case of the traditional model using a constant C_s, the value of k is overestimated in the downstream free shear layer, as is shown in Fig. 19 (2). This is caused by an inadequate value of C_s. C_s is set 0.12 throughout the space for the case shown in Fig. 19 (2). However C_s should naturally take a larger value in the free shear layer. In the case of variable C_s, the overestimation of k in the free shear layer tends to be rectified, as shown in Fig.19 (3). The value of C_s at this area is about 0.14 as is shown in Fig. 18. This value is more adequate than 0.12 for this region.

8. COMPARISON OF DIFFERENT TURBULENCE MODELS FOR VARIOUS FLOWFIELDS

There exist various types of flow in the field of building engineering, e.g. with and without curvature effect, buoyant (isothermal) or non-buoyant (non-isothermal), stable and unstable etc. The flowfield around a bluff body is characterized by a strong curvature effect which is caused by impinging and separation. The diffusion of smoke from a stack is a buoyant flow. The heat loss due to wind exposure is a phenomenon of heat transfer.

No turbulence model can be entirely free from some type of shortcoming caused by the modelling procedure, whether it be serious or non-serious. The shortcomings caused by EVM for k-ε and algebraic approximation for ASM have been described above.

Table 1 Relative comparison of various turbulence models for practical modelling of flowfields related building engineering

Turbulence model	Standard k − ε	Low-Re. No. k − ε	Standard DSM (ASM)	Low-Re. No. DSM (ASM)	LES	LES
wall boundary condition	wall function	non-slip	wall function	non-slip	wall function	non-slip
1. Simple flows (channel flow, pipe flow, etc) (local equilibrium is valid)	○	○	○	○	○	○
2. Flow with streamline curvature 1) weak curvature 2) strong curvature (flow around bluff body)	○ ×, △	○ ×, △	○ ○	○ ○	○ ○	○ ○
3. Impinging flow	×, △	×, △	△, ○	△, ○	○	○
4. Flowfield with low Reynolds No.	×, △	△, ○	×, △	△, ○	○	○
5. Non − isothermal flow 1) weak stratification 2) strong stratification	○ ×, △	○ ×, △	○ ○	○ ○	○ ○	○ ○
6. Convective heat transfer at wall	×, △	○	×, △	○	×, △	○
7. Unsteady flow, unsteady diffusion 1) highly unsteady 2) vortex shedding	× ×	× △	× ○	× ○	○ ○	○ ○
8. Jet 1) normal 2) swirl	○ ×	○ ×	○ ○	○ ○	○ ○	○ ○

○ : functions well △ : insufficiently functional × : functions poorly

Therefore, when analyzing a specific problem, we should select the proper turbulence model. An improvement in prediction accuracy is usually followed by an increase of CPU time and calculation instability. Thus a strategy for selecting a turbulence model may be proposed according to the purpose of the analysis and the accuracy required. The relative abilities of various turbulence models are compared in Table 1. The well-known k–ε model is most widely used for the analysis of mean flowfields. When a flowfield is highly anisotropic, DSM or ASM are applied successfully. For an analysis of unsteady flowfield, LES can be used.

The flow pattern around a bluff body can be predicted by k–ε with a certain accuracy. However, for reproducing surface pressure and turbulence statistics such as $\langle u'_i u'_j \rangle$, analysis by ASM (or DSM) or LES is effective. LES provides greater estimation accuracy than the other turbulence models but requires much more CPU time.

9. CONCLUSION

1. The flowfield around a bluff body is characterized by the complex distribution of strain-rate tensor $\frac{\partial \langle u_i \rangle}{\partial x_j}$ around it. Therefore the distributions of surface pressure, Reynolds stress and production terms are also very complicated.
2. The flowfield around a cube as predicted by LES, ASM and k–ε EVM are compared precisely with the experimental data, and the accuracy of each model is examined. The shortcomings included in k–ε EVM and ASM are thus clarified.
3. A new model of LES with variable Smagorinsky constant is presented.

ACKNOWLEDGEMENTS

The numerical studies using the $k-\varepsilon$ model, ASM and LES were carried out in cooperatio with Dr. A. Mochida and Mr. Y. Tominaga (I.I.S., Univ. of Tokyo). This paper was written with th assistance of Mr. Y. Tominaga. The author would like to express his gratitude for their valuabl contributions to this work.

NOMENCLATURE

x_i : three components of spatial coordinate (i = 1,2,3 : streamwise, lateral, vertical)
$<f>$: time-averaged value of f
$\bar{f}$: filtered value of f
f' : deviation from $<f>$, $f'=f-<f>$ (In LES, $f'=\bar{f}-<\bar{f}>$)
f'' : deviation from $\bar{f}$, $f''=f-\bar{f}$
H_b : height of cube
u_i : three components of velocity vector
u_b : u_1 value at inflow of computational domain at height H_b
p : pressure
ν_t : eddy viscosity
ν_{SGS} : subgrid scale eddy viscosity
k : turbulent kinetic energy, $k = \frac{1}{2} <u_i'u_i'>$
k_{sgs} : subgrid component of k, $k_{sgs}=\frac{1}{2}\overline{u_i''u_i''}$
S_{ij} : strain rate tensor, $S_{ij}=\left(\frac{\partial<u_i>}{\partial x_j}+\frac{\partial<u_j>}{\partial x_i}\right)$, $(S=[\frac{1}{2}(S_{ij})^2]^{1/2})$
P_k : production of k
ε : dissipation rate of k
$<u_i'u_j'>$: Reynolds stress
P_{ij} : production of $<u_i'u_j'>$
ε_{ij} : dissipation rate of $<u_i'u_j'>$
C_{ij} : convection term of $<u_i'u_j'>$,
D_{ij} : diffusion term of $<u_i'u_j'>$, $D_{ij}=\frac{\partial}{\partial x_k}(-<u_i'u_j'u_k'>-<p'u_i'>\delta_{jk}-<p'u_j'>\delta_{ik})$
Φ_{ij} : pressure-strain correlation term (consists of $\Phi_{ij(1)}$, $\Phi_{ij(2)}$, $\Phi^{w}_{ij(1)}$ and $\Phi^{w}_{ij(2)}$)
h_i : mesh interval in x_i direction
h : mesh scale, $h=(h_1h_2h_3)^{1/3}$
h_P : mesh interval adjacent to solid wall
$(u_i)_P$: tangential component of velocity vector at the near-wall node
k_P : k value at the near-wall node
ε_P : ε value at the near-wall node
τ_W : wall shear stress
$h_n^{(w)}$: vertical distance from the w-th wall
Re : Reynolds number ($<u_b>H_b/\nu = 8.4 \times 10^4$)
Values are made dimensionless by $<u_b>$, H_b and air density ρ.

Note 1 Model equations and numerical methods

The standard formulation for $k-\varepsilon$ EVM [11, 12] was adopted (Appendix 1). The model equations for ASM are shown in Appendix 2. The commonly adopted form for ASM was used, following the methods of Rodi,W.[15], Gibson,M.M. and Launder,B.E.[16] except for the treatment of the wall reflection term $\Phi^{w}_{ij(2)}$ [17, 20]. The values of the numerical constants in ASM follow those proposed by Launder,B.E.,Reece,G.J. and Rodi,W.[18] and Launder,B.E.[19] In LES, the Smagorinsky subgrid model [13, 14] was applied and the value of 0.12 was selected for the Smagorinsky constant C_s (Appendix 3).

A staggered grid was adopted. A second-order upwind scheme (the QUICK scheme) was applied for the convection terms in the cases of $k-\varepsilon$ EVM and ASM. A second-order centered difference scheme was adopted for the other spatial derivatives. The Adams-Bashforth scheme was used for time marching.

Note 2 Mesh arrangements and boundary conditions

The computational domain covered 15.7 (x_1 direction), 9.7 (x_2 direction) and 5.2 (x_3 direction). This domain was discretized into 50 (x_1) × 49 (x_2) × 28 (x_3) meshes for the cases of $k-\varepsilon$ EVM and ASM, and 63 (x_1) × 49 (x_2) × 34 (x_3) meshes for the case of LES. The minimum mesh interval in the area around the frontal corner of the cube was set at 1/24 for all cases.

Boundary conditions are summarized in Table ①. For the inflow boundary of LES, time history of $\overline{u_i(t)}$ in a fully developed channel flow predicted by LES was utilized. The profiles of $\langle\overline{u_i(x_3)}\rangle$ and $k(x_3)$ in the boundary layer of the channel given by LES correspond well to those of the experiment [20].For the boundary conditions at the solid walls, the generalized logarithmic law expressed by eq.① [12] was employed in order to estimate the time-averaged wall shear stress $\langle\tau_w\rangle$ for the cases of three models. Furthermore, eq.④ was used to specify the instantaneous wall shear stress τ_w for the case of LES. As shown in Table ①, almost the same boundary conditions were imposed for the calculations of the all three models so far as the time averaged flowfields were concerned. Therefore, it can be concluded that the differences observed in the results from these three models are mainly caused by the differences in turbulence modellings.

Table ① Boundary conditions

	k–ε EVM, ASM	LES
inflow	$\langle u_1(x_3)\rangle$: $\langle u_1(x_3)\rangle \fallingdotseq x_3^{1/4}$ (measured profile in wind tunnel) $\langle u_2(x_3)\rangle = 0$, $\langle u_3(x_3)\rangle = 0$ $k(x_3)$: predicted distribution in plane channel by LES (this distribution corresponds well to that measured in the experiment [20]) $\nu_t(x_3) = k(x_3)^{1/2}\ell(x_3)$, $\varepsilon(x_3) = C_\mu k(x_3)^{3/2}/\ell(x_3)$ $\ell(x_3) = (C_\mu k(x_3))^{1/2}\{(\partial\langle u_1\rangle/\partial x_3)^{-1}\}$ $(P_k(x_3) = \varepsilon(x_3))$ $\langle u_1'^2(x_3)\rangle = \frac{2}{3}k(x_3)$	$\overline{u_1(t)}$, $\overline{u_2(t)}$, $\overline{u_3(t)}$: time history of velocity in boundary layer of plane channel predicted by LES. $\begin{pmatrix}\langle\overline{u_1(x_3)}\rangle \fallingdotseq x_3^{1/4}\\ \langle\overline{u_2(x_3)}\rangle = 0\\ \langle\overline{u_3(x_3)}\rangle = 0\end{pmatrix}$
outflow	$\langle u_1\rangle$, $\langle u_2\rangle$, $\langle u_3\rangle$, k, ε : free slip $(\partial/\partial x_1 = 0)$	$\overline{u_1}$, $\overline{u_2}$, $\overline{u_3}$: free slip
upper face of computational domain	$\langle u_3\rangle = 0$, $\langle u_1\rangle$, $\langle u_2\rangle$, k, ε : free slip $(\partial/\partial x_3 = 0)$	$\overline{u_3} = 0$, $\overline{u_1}$, $\overline{u_2}$: free slip
side faces of computational domain	$\langle u_2\rangle = 0$, $\langle u_1\rangle$, $\langle u_3\rangle$, k, ε : free slip $(\partial/\partial x_2 = 0)$	$\overline{u_2} = 0$, $\overline{u_1}$, $\overline{u_3}$: free slip
solid wall	The time averaged wall shear stress $\langle\tau_w\rangle$ is given by equation ①. The volume averaged value of ε at the near – wall grid used for transport equation of k is expressed by equation②, and defined as $\bar{\varepsilon}$. The value of ε at the near – wall node used for transport equation of ε is defined by equation ③. $\frac{\langle(u_t)_P\rangle}{\langle\tau_w\rangle}(C_\mu^{1/4}k_P)^{1/2} = \frac{1}{\kappa}ln\left(\frac{E\cdot\frac{1}{2}h_P(C_\mu^{1/4}k_P)^{1/2}}{\nu}\right)\cdots①$ $\bar{\varepsilon} = \frac{C_\mu^{3/4}\cdot k_P^{3/2}}{\kappa h_P}ln\left(\frac{Eh_P(C_\mu^{1/4}k_P)^{1/2}}{\nu}\right)\cdots②$ $\varepsilon_P = \frac{C_\mu^{3/4}\cdot k_P^{3/2}}{\frac{1}{2}\kappa h_P}\cdots③$ k : free slip $(\kappa=0.4, C_s=0.09, E=9.0)$	$\tau_w = \langle\tau_w\rangle \times \frac{\overline{(u_t)_P}}{\langle(u_t)_P\rangle}$ $\cdots④$ $\langle\tau_w\rangle$ is estimated by equation①. $\langle(u_t)_P\rangle$, k_P are given by using the results of the foregoing time steps.

Appendix 1 Model equations for k–ε EVM

$$\frac{\partial\langle u_i\rangle}{\partial t}+\frac{\partial\langle u_i\rangle\langle u_j\rangle}{\partial x_j}=-\frac{\partial\langle p\rangle}{\partial x_i}+\frac{\partial}{\partial x_j}\nu_t\left(\frac{\partial\langle u_i\rangle}{\partial x_j}+\frac{\partial\langle u_j\rangle}{\partial x_i}\right) \quad (1.1)$$

$$\frac{\partial\langle u_i\rangle}{\partial x_i}=0 \quad (1.2)$$

$$\frac{\partial k}{\partial t}+\frac{\partial k\langle u_j\rangle}{\partial x_j}=\frac{\partial}{\partial x_j}\left(\frac{\nu_t}{\sigma_k}\frac{\partial k}{\partial x_j}\right)+\nu_t\left(\frac{\partial\langle u_i\rangle}{\partial x_j}+\frac{\partial\langle u_j\rangle}{\partial x_i}\right)\frac{\partial\langle u_i\rangle}{\partial x_j}-\varepsilon \quad (1.3)$$

$$\frac{\partial\varepsilon}{\partial t}+\frac{\partial\varepsilon\langle u_j\rangle}{\partial x_j}=\frac{\partial}{\partial x_j}\left(\frac{\nu_t}{\sigma_\varepsilon}\frac{\partial\varepsilon}{\partial x_j}\right)+\frac{\varepsilon}{k}\left(C_{\varepsilon1}\nu_t\left(\frac{\partial\langle u_i\rangle}{\partial x_j}+\frac{\partial\langle u_j\rangle}{\partial x_i}\right)\frac{\partial\langle u_i\rangle}{\partial x_j}-C_{\varepsilon2}\varepsilon\right) \quad (1.4)$$

$$-\langle u_i'u_j'\rangle=\nu_t\left(\frac{\partial\langle u_i\rangle}{\partial x_j}+\frac{\partial\langle u_j\rangle}{\partial x_i}\right)-\frac{2}{3}\delta_{ij}k \quad (1.5)$$

$$\nu_t=C_\mu\frac{k^2}{\varepsilon} \quad (1.6)$$

C_μ : 0.09, σ_k : 1.0, σ_ε : 1.3, $C_{\varepsilon1}$: 1.44, $C_{\varepsilon2}$: 1.92

Appendix 2 Model equations for ASM (DSM)

$$\frac{\partial\langle u_i\rangle}{\partial t}+\frac{\partial\langle u_i\rangle\langle u_j\rangle}{\partial x_j}=-\frac{\partial\langle p\rangle}{\partial x_i}-\frac{\partial\langle u_i'u_j'\rangle}{\partial x_j} \quad (2.1)$$

$$\frac{\partial\langle u_i\rangle}{\partial x_i}=0 \quad (2.2)$$

$$\frac{\partial k}{\partial t}+\frac{\partial k\langle u_j\rangle}{\partial x_j}=D_k+P_k-\varepsilon \quad (2.3)$$

$$\frac{\partial\varepsilon}{\partial t}+\frac{\partial\varepsilon\langle u_j\rangle}{\partial x_j}=D_\varepsilon+\frac{\varepsilon}{k}(C_{\varepsilon1}P_k-C_{\varepsilon2}\varepsilon) \quad (2.4)$$

$$\frac{\partial\langle u_i'u_j'\rangle}{\partial t}+\frac{\partial\langle u_i'u_j'\rangle\langle u_l\rangle}{\partial x_l}=D_{ij}+P_{ij}+\Phi_{ij}-\varepsilon_{ij} \quad (2.5)$$

$$(P_k-\varepsilon)\frac{\langle u_i'u_j'\rangle}{k}=P_{ij}+\Phi_{ij}-\varepsilon_{ij} \quad \text{(in case of ASM)} \quad (2.6)$$

$$D_k=\frac{\partial}{\partial x_m}\left(C_k\langle u_m'u_l'\rangle\cdot\frac{k}{\varepsilon}\cdot\frac{\partial k}{\partial x_l}\right) \quad (2.7)$$

$$D_\varepsilon=\frac{\partial}{\partial x_m}\left(C_\varepsilon\langle u_m'u_l'\rangle\cdot\frac{k}{\varepsilon}\cdot\frac{\partial\varepsilon}{\partial x_l}\right) \quad (2.8)$$

$$P_k=-\langle u_i'u_j'\rangle\frac{\partial\langle u_i\rangle}{\partial x_j} \quad (2.9)$$

$$D_{ij}=\frac{\partial}{\partial x_m}\left(C_k\langle u_m'u_l'\rangle\cdot\frac{k}{\varepsilon}\cdot\frac{\partial\langle u_i'u_j'\rangle}{\partial x_l}\right) \quad (2.10)$$

$$P_{ij}=-\langle u_i'u_k'\rangle\frac{\partial\langle u_j\rangle}{\partial x_k}-\langle u_j'u_k'\rangle\frac{\partial\langle u_i\rangle}{\partial x_k} \quad (2.11)$$

$$\varepsilon_{ij}=\frac{2}{3}\cdot\delta_{ij}\varepsilon \quad (2.12)$$

$$\Phi_{ij}=\Phi_{ij(1)}+\Phi_{ij(2)}+\Phi_{ij(1)}^{w}+\Phi_{ij(2)}^{w} \quad (2.13)$$

$$\Phi_{ij(1)}=-C_1\frac{\varepsilon}{k}\left(\langle u_i'u_j'\rangle-\frac{2}{3}\delta_{ij}k\right) \quad (2.14)$$

$$\Phi_{ij(2)}=-C_2\left(P_{ij}-\frac{2}{3}\delta_{ij}P_k\right) \quad (2.15)$$

$$\Phi_{ij(1)}^{w}=\sum_{w=1}^{w0}C_1'\frac{\varepsilon}{k}\left(\langle u_k'u_m'\rangle\cdot n_k^{(w)}\cdot n_m^{(w)}\cdot\delta_{ij}-\frac{3}{2}\langle u_k'u_i'\rangle\cdot n_k^{(w)}\cdot n_j^{(w)}-\frac{3}{2}\langle u_k'u_j'\rangle\cdot n_k^{(w)}\cdot n_i^{(w)}\right)\cdot\frac{k^{3/2}}{C_l\cdot h_n^{(w)}\varepsilon} \quad (2.16)$$

$$\Phi_{ij(2)}^{w}=\sum_{w=1}^{w0}C_2'\left(\Phi_{km(2)}\cdot n_k^{(w)}\cdot n_m^{(w)}\cdot\delta_{ij}-\frac{3}{2}\Phi_{ik(2)}\cdot n_k^{(w)}\cdot n_j^{(w)}-\frac{3}{2}\Phi_{kj(2)}\cdot n_k^{(w)}\cdot n_i^{(w)}\right)\cdot\frac{k^{3/2}}{C_l\cdot h_n^{(w)}\varepsilon} \quad (2.17)$$

C_μ : 0.09, σ_k : 1.0, σ_ε : 1.3, C_1 : 1.8, C_2 : 0.6, C_1' : 0.5, C_2' : 0.5, C_k : 0.22, C_ε : 0.16, $C_{\varepsilon1}$: 1.44, $C_{\varepsilon2}$: 1.92, C_l : 2.5

Appendix 3 Model equations for LES

1) Traditional model

$$\frac{\partial \overline{u_i}}{\partial t}+\frac{\partial \overline{u_i}\,\overline{u_j}}{\partial x_j}=-\frac{\partial \overline{p}}{\partial x_i}+\frac{\partial}{\partial x_j}(\nu+\nu_{SGS})\left(\frac{\partial \overline{u_i}}{\partial x_j}+\frac{\partial \overline{u_j}}{\partial x_i}\right) \quad (3.1)$$

$$\frac{\partial \overline{u_i}}{\partial x_i}=0 \quad (3.2)$$

$$\nu_{SGS}=(C_{S0}\,h)^2 S \quad (3.3)$$

$$h=(h_1 h_2 h_3)^{1/3} \quad (3.4)$$

$$S=\left\{\frac{\partial \overline{u_i}}{\partial x_j}\left(\frac{\partial \overline{u_i}}{\partial x_j}+\frac{\partial \overline{u_j}}{\partial x_i}\right)\right\}^{1/2} \quad (3.5)$$

C_{S0} : 0.12 (3.6)

2) New model with variable Smagorinsky constant (cf. Appendix 4)

$$\nu_{SGS}=(C_S h)^2 S \quad (3.7)$$

$$\frac{C_S}{C_{S0}}=1-C_A\frac{(DS/Dt)}{S^2} \quad (3.8)$$

$C_A=1.8$, $C_{S0}=0.16$

$C_{S,min}\leq C_S\leq C_{S,max}$, $C_{S,min}=0.10$, $C_{S,max}=0.27$

Appendix 4 Derivation of new model of LES with variable Smagorinsky Constant [22]

The transport equation of k_{SGS} is expressed as follows.

$$\frac{Dk_{SGS}}{Dt}=D_{k_{SGS}}+P_{k_{SGS}}-\varepsilon \quad (4.1)$$

Eq.(4.1) is transformed as follows.

$$\varepsilon=P_{k_{SGS}}\left\{1-\frac{(Dk_{SGS}/Dt)}{P_{k_{SGS}}}+\frac{D_{k_{SGS}}}{P_{k_{SGS}}}\right\}, \quad (4.2)$$

where $P_{k_{SGS}}$: production term of k_{SGS}, $\nu_{SGS}S^2$ (4.3)

$D_{k_{SGS}}$: diffusion term of k_{SGS}, $\frac{\partial}{\partial x_j}\left(\frac{\nu_{SGS}}{\sigma_{k_{SGS}}}\frac{\partial k_{SGS}}{\partial x_j}\right)$ (4.4)

$S=\left\{\frac{1}{2}(S_{ij})^2\right\}^{1/2}$, S_{ij} is a strain rate tensor (4.5)

$\sigma_{k_{SGS}}=1$

Dimensional analysis gives the followings.

$$\nu_{SGS}=C_1\Delta^{3/4}\varepsilon^{1/3}$$

$$k_{SGS}=C_2\Delta^{4/3}\varepsilon^{2/3}, \quad (4.6)$$

here Δ means SGS length scale. (4.7)

Eq.(4.2) is expressed as eq.(4.8) in terms of eqs.(4.3) ~ (4.7).

$$\varepsilon=C_1^{3/2}\Delta^2 S^3\left[1-\frac{2}{3}C_1^{-1}C_2\Delta^{-2/3}\varepsilon^{-2/3}S^{-2}\frac{D\varepsilon}{Dt}+\frac{2}{3}C_2\Delta^{-2/3}\varepsilon^{-1/3}S^{-2}\frac{\partial \varepsilon}{\partial x_j}\right]^{3/2} \quad (4.8)$$

In the derivation of traditional Smagorinsky model, local equilibrium is assumed and hence the second and third terms in the blacket of eq.(4.8) are neglected. Thus

$$\varepsilon=C_1^{3/2}\Delta^2 S^3 \quad (4.9)$$

The effects of advection and diffusion of k_{SGS} are thus not included in the traditional model.

Traditional Smagorinsky model is given from eq.(4.6) and (4.9) as follows.

$$\nu_{SGS}=(2C_1^{3/4}\Delta)^2 S=(C_{S0}\Delta)^2 S$$

here $C_{S0}=2C_1^{3/4}$ (4.10)

C_{S0} is set to be 0.12 for the simulation with traditional model in this paper.

The new model of LES with variable Smagorinsky constant is derived as follows.

After evaluating the second and third terms in the bracket of eq.(4.8) by means of eq.(4.9), eq.(4.11) is given by eliminating ε with the aid of eq.(4.6)

$$\nu_{SGS}=\underline{\left[2C_1^{3/4}\left\{1-2C_1^{-1/2}C_2S^{-2}\frac{DS}{Dt}+8C_1C_2\Delta^2S^{-3}\frac{\partial}{\partial x_j}\left(S^2\frac{\partial S}{\partial x_j}\right)\right\}^{1/4}\Delta\right]^2 S} \quad (4.11)$$

When the part underlined is expressed as C_S,

$$\nu_{SGS}=(C_S\Delta)^2 S \quad (4.12)$$

This expression is an original form of ν_{SGS}.

Here C_S is defined as a function of time and space as follows.

$$\frac{C_S}{C_{S0}}=\left[1-2C_1^{-1/2}C_2S^{-2}\frac{DS}{Dt}+8C_1C_2\Delta^2S^{-3}\frac{\partial}{\partial x_j}\left(S^2\frac{\partial S}{\partial x_j}\right)\right]^{1/4},$$

here $C_{S0}=2C_1^{3/4}$ (4.13)

This is the definition of the model with variable Smagorinsky constant.

Eq.(4.13) is transformed as eq.(4.14).

$$\frac{C_S}{C_{S0}}=1-C_AS^{-2}\frac{DS}{Dt}+C_B\Delta^2S^{-3}\frac{\partial}{\partial x_j}\left(S^2\frac{\partial S}{\partial x_j}\right), \quad (4.14)$$

here $C_A=\frac{1}{2}C_1^{-1/2}C_2$, $C_B=2C_1C_2$

The values of the constant are given by A. Yoshizawa by means of statistical theory of a two-scale DIA.

$$C_1\fallingdotseq 0.035,\ C_2\fallingdotseq 0.67, \qquad (4.15)$$

here Δ is set to be $2h$.

Thus, C_A, C_B, C_{S0} in eq.(4.14) are given as follows.

$$C_A=1.8,\ C_B=0.047,\ C_{S0}=0.16 \qquad (4.16)$$

in this paper we neglect the diffusion term since its effect seems to be small, thus (3.8) in Appendix 3 is given. Furthermore the maximum and minimum values of C_s are imposed as follows, for the convenience of calculation stability [21].

$$C_{s,max}=0.27,\ C_{s,min}=0.10 \qquad (4.17)$$

REFERENCES

1 D.A.Paterson and C.J.Apelt, Simulation of flow past a cube in a turbulent boundary layer, J.Wind Eng.Ind.Aerodyn., 35 (1990) 149 – 176.

2 S.Murakami and A.Mochida, 3D numerical simulation of airflow around a cubic model by means of k-ε model, J.Wind Eng.Ind.Aerodyn., 31 (1988) 283 – 303.

3 F.Baetke,H.Werner and H.Wengle, Numerical simulation of turbulent flow over surface-mounted obstacles with sharp edges and corners, J.Wind Eng.Ind. Aerodyn., 35 (1990) 129 – 147.

4 S.Murakami, Computational wind engineering, J.Wind Eng.Ind.Aerodyn., 36 (1990) 517 – 538

5 T.Stathopoulos and A.Baskaran, Boundary treatment for the computational of three-dimensional wind flow conditions around a building, J.Wind Eng.Ind. Aerodyn., 35 (1990) 177 – 200.

6 S.Murakami and A.Mochida,Numerical simulations of air flow around surface-mounted square rib by means of ASM and k-ε EVM,ASCE 9th Structures Congress (1991) 639 – 642.

7 S.Murakami,A.Mochida and K.Hibi, Three-dimensional numerical simulation of airflow around a cubic model by means of large eddy simulation, J.Wind Eng.Ind.Aerodyn., 25 (1987) 291 – 305.

8 S.Murakami,A.Mochida,Y.Hayashi and S.Sakamoto, Numerical study on velocity-pressure field and wind forces for bluff bodies by k-ε ,ASM and LES, 8th Int. Conf. on Wind Eng, London,Canada (1987).

9 S.Murakami,A.Mochida and Y.Hayashi, examining the k-ε model by means of a wind tunnel test and large-eddy simulation of the turbulence structure around a cube, J.Wind Eng.Ind.Aerodyn., 35 (1990) 87 – 100.

10 T.Tamura,I.Ohta and K.Kuwahara, On the reliability of two-dimensional simulation for unsteady flows around a cylinder-type structure, J.Wind Eng. Ind.Aerodyn., 35 (1990) 275 – 298.

11 B.E.Launder and D.B.Spalding, Mathematical models of turbulence, Academic Press, New York, 1972.

12 B.E.Launder and D.B.Spalding, The numerical computation of turbulent flows, Comput. Methods Appl.Mech.Eng., 3 (1974) 269 – 289.

13 J.Smagorinsky, General circulation experiments with the primitive equations, Part1, Basic experiments,Mon.Weather Rev., 91 (1963) 99 – 164.

14 J.W.Deardorff, A numerical study of three-dimensional turbulent channel flow at large Reynolds numbers, J.Fluid Mech., 41 (1970) 453 – 480.

15 W.Rodi, ZAMM, 58 (1976) T219 – T221.

16 M.M.Gibson and B.E.Launder, Ground effects on pressure fluctuations in the atmospheric boundary layer, J.Fluid Mech., 86 (1978) 491 – 511.

17 S.Murakami,S.Kato and Y.Kondo, Examining k-ε EVM by means of ASM for a 3 – D horizontal buoyant jet in enclosed space, Int. Symp. on Engineering Turbulence Modelling and Experiments, Dubrovnik, Yugoslavia,(1990) 205-214.

18 B.E.Launder,G.J.Reece and W.Rodi, Progress in the development of a Reynolds stress turbulence closure, J.Fluid Mech., 68 (1975) 537 – 566.

19 B.E.Launder, University of Manchester, Institute of Science and Technology, Report No.TFD/82/4, 1983

20 S.Murakami,A.Mochida and Y.Hayashi, Scrutinizing k-ε EVM and ASM by means of LES and wind tunnel for flowfield around cube, 8th Symp. on Turbulent Shear Flows (1991).

21 Y.Morinishi and T.Kobayashi, Large eddy simulation of backward facing step flo
on Engineering Turbulence Modelling and Experiments, Dubrovnik, Yugoslavia,(1990
22 A.Yoshizawa, Eddy-viscosity-type subgrid-scale model with a variable Smagorinsky
and its relationship with the one-equation model in large eddy simulation, Phys.F
(1991),2007-2009.
23 K.Mizutani, S.Murakami, S.Kato, A.Mochida, Numerical Simulation of Room Air Flo
of Large Eddy Simulation (Part1and2), Summaries of Technical Papers of Annua
Artitechtural Institute of Japan, Environ. Eng., 483-486.(in Japanese).